





Splicing the active phases of copper/cobalt-based catalysts achieves high-rate tandem electroreduction of nitrate to ammonia

Wenhui He¹, Jian Zhang ¹, Stefan Dieckhöfer¹, Swapnil Varhade¹, Ann Cathrin Brix ¹, Anna Lielpetere¹, Sabine Seisel ¹, João R. C. Junqueira¹ & Wolfgang Schuhmann ¹✉

Electrocatalytic recycling of waste nitrate (NO_3^-) to valuable ammonia (NH_3) at ambient conditions is a green and appealing alternative to the Haber–Bosch process. However, the reaction requires multi-step electron and proton transfer, making it a grand challenge to drive high-rate NH_3 synthesis in an energy-efficient way. Herein, we present a design concept of tandem catalysts, which involves coupling intermediate phases of different transition metals, existing at low applied overpotentials, as cooperative active sites that enable cascade NO_3^- -to- NH_3 conversion, in turn avoiding the generally encountered scaling relations. We implement the concept by electrochemical transformation of Cu–Co binary sulfides into potential-dependent core–shell Cu/CuO_x and Co/CoO phases. Electrochemical evaluation, kinetic studies, and in-situ Raman spectra reveal that the inner Cu/CuO_x phases preferentially catalyze NO_3^- reduction to NO_2^- , which is rapidly reduced to NH_3 at the nearby Co/CoO shell. This unique tandem catalyst system leads to a NO_3^- -to- NH_3 Faradaic efficiency of $93.3 \pm 2.1\%$ in a wide range of NO_3^- concentrations at pH 13, a high NH_3 yield rate of $1.17 \text{ mmol cm}^{-2} \text{ h}^{-1}$ in 0.1 M NO_3^- at -0.175 V vs. RHE , and a half-cell energy efficiency of $\sim 36\%$, surpassing most previous reports.

¹Analytical Chemistry—Center for Electrochemical Sciences (CES), Faculty of Chemistry and Biochemistry, Ruhr University Bochum, Universitätsstr. 150, 44780 Bochum, Germany. ✉email: wolfgang.schuhmann@rub.de

Ammonia (NH₃) is the critical feedstocks of artificial fertilizers and various chemicals and one of the most promising carbon-free energy carriers^{1–3}. Currently, industrial NH₃ synthesis heavily relies on the energy and carbon-emission intensive Haber–Bosch (H–B) process^{4–7}. Alternatively, electrocatalytic N₂-to-NH₃ conversion (eN₂-NH₃), using water (H₂O) as a proton source, has recently attracted significant research interests owing to its mild conditions and high compatibility with renewable electricity^{6,8–15}. However, the inherent characters of N₂, including high dissociation energy of the N≡N bond (945 kJ mol⁻¹) and low water solubility, make the eN₂-NH₃ work at an insufficient selectivity and two orders of magnitude lower yield rate than that of H–B process^{9–11,16}. To bridge the gap, the knowledge of the nitrogen cycle brings a renewed attention to the recycling of reactive N-containing species (e.g., NO and nitrate) to NH₃^{17–20}. Among them, the nitrate (NO₃⁻) anion is particularly attractive because it exhibits comparatively low dissociation energy of the N=O bond (204 kJ mol⁻¹) and is widely abundant as pollution in agricultural and industrial wastewaters^{20–26}. Furthermore, initial developments of plasma techniques promise to convert air to NO₃⁻ with low energy consumption^{27,28}. Therefore, using NO₃⁻ as the precursor endows NH₃ electrosynthesis with sustainable features and opens up an economical route to remedy environmental pollution.

NO₃⁻-to-NH₃ conversion in microorganisms is a tandem process; i.e., NO₃⁻ reduction to NO₂⁻ using nitrate reductase and subsequent NO₂⁻-to-NH₃ conversion employing nitrite reductase or nitrogenase, independently^{29–31}. This enzyme-based tandem system allows efficient NH₃ generation at ambient conditions in nature owing to its specific coordination binding with NO₃⁻ and NO₂⁻, respectively^{29,31,32}. However, NO₃⁻ typically shows low binding affinity to transition metals in aqueous electrolytes due to its symmetrical (D_{3h}) resonant structure and strong hydrogen bonding to H₂O^{31,33,34}. Moreover, the NO₃⁻-to-NH₃ pathway involves a complex eight-electrons transfer and multiple intermediates^{17,35,36}. As a result, there is a scaling relation between the binding strengths of NO₃⁻, NO₂⁻ and other oxygen-containing intermediates (e.g., NO) on the transition metal surface³⁷. Optimizing the adsorption of one species will typically take the others away from their optima^{38,39}, making the simultaneous acceleration of sequential NO₃⁻-to-NO₂⁻ and NO₂⁻-to-NH₃ reactions considerably challenging.

Copper (Cu)-based catalysts have been intensively investigated for the NO₃⁻ reduction reaction (NO₃RR) due to its favorable ability to bind NO₃⁻ and catalyze NO₃⁻-to-NO₂⁻ conversion^{40–43}. However, pure Cu catalysts commonly suffer from rapid deactivation because of their strong adsorption of the NO₃RR intermediates (e.g., NO₂⁻ and NO)^{42–44}. Substantial efforts have recently been made to alleviate these limitations by regulating the proton- and/or electron-transfer, as well as the binding strengths of partially reduced intermediates adsorbed on Cu centres. This was performed either by alloying Cu with noble or other transition metals (e.g., Pt, Pd and Ni)^{40,45–49} or through the formation of hybrids with molecular solids or metal oxides (e.g., Cu₂O)^{44,50,51}. These strategies have increased the Faradaic efficiency (FE) of NH₃ to an impressive 70–100% and the NH₃ yield rate (Y_{NH₃}) to a level of 30–200 μmol cm⁻² h⁻¹^{44,45,51}. However, restricted by the scaling relations, these advances require highly concentrated NO₃⁻ (e.g., 1 M) and/or relatively high overpotentials (<–0.4 V vs. RHE) to balance the rates of NO₃⁻-to-NO₂⁻ and NO₂⁻-to-NH₃ reactions, resulting in an increased energy consumption^{44,45,51}. To compete with the H–B process, further progress on Y_{NH₃} (>1 mmol cm⁻² h⁻¹)⁵² and on decreasing energy consumption are highly desirable.

Energy-efficient NO₃RR points to low operating overpotentials (e.g., >–0.2 V vs. RHE), at which transition metal (e.g., Cu and

Co)-based catalysts often suffer from potential-dependent phase evolution, leading to the coexistence of multiple phases, such as metallic, oxide and hydroxide phases^{53–56}. In situ monitoring of the phase evolution of transition metals during the NO₃RR, while correlating these intermediate phases with specific catalytic steps^{53,54,57,58}, may not only guide the rational design of selective catalysts for NH₃ but also provide insight into the NO₃RR. Inspired by the tandem NO₃⁻-to-NH₃ conversion in nature²⁹, we sought, therefore, to circumvent the scaling relations by combining two or more cooperative intermediate phases exhibiting complementary catalytic selectivity into one tandem system, intending to achieve NH₃ synthesis at low overpotentials. Importantly, it has been clearly demonstrated that the reaction rate and selectivity of a tandem catalyst system, linked to the transport of key intermediates, could be optimized by judiciously tuning the proximity, hierarchy and content ratio of multiple active phases^{39,59–62}. Accordingly, the Y_{NH₃} could be further improved, however, to the best of our knowledge, tandem catalysts based on earth-abundant elements have never been reported for electrocatalytic consecutive NO₃⁻-to-NH₃ conversion.

In this work, we introduce a facile electrochemically driven phase-separation strategy for a tandem catalyst design, which, different from previous approaches based on sequential assembling or deposition^{60,61}, enables the in situ formation of multiple active intermediate phases and rich phase interfaces for rapid spillover and transport of reaction intermediates. As a proof-of-concept, we implemented this catalyst synthesis strategy by the electrochemical transformation of pre-synthesized Cu–Co binary metal sulfides into core-shell Cu/CuO_x and Co/CoO phases on Cu foil. The employment of Co-based phases as a sub-component of the tandem catalysts was inspired by the previously reported high selectivity of Co-based materials and complexes for NH₃ generation during the NO₃RR and the specific NO₂⁻-to-NH₃ conversion^{63,64}. Our electrocatalytic tests, kinetic studies, in situ scanning electrochemical microscopy (SECM) and in situ Raman spectra reveal that at low overpotentials, the inner Cu/CuO_x phases preferentially catalyze NO₃⁻ reduction to NO₂⁻, while the outer-layer Co/CoO phases selectively catalyze NO₂⁻ reduction to NH₃, both of which can be combined for rapid “working-in-tandem” NH₃ synthesis. As a result, we report NO₃⁻-to-NH₃ conversion with a FE of 93.3 ± 2.1% in a wide range of NO₃⁻ concentrations at –0.175 V vs. RHE, a high NH₃ yield rate of 1.17 mmol cm⁻² h⁻¹ in 0.1 M NO₃⁻ at pH 13 and a half-cell energy efficiency of ~36%, which surpass most prereports.

Results

Catalyst design and characterization. The synthesis of Cu/Co-based tandem catalysts is schematically illustrated in Fig. 1a. A nanorod array of metal-organic frameworks (MOFs) was first grown on Cu foil by optimizing the molar ratio of 2-methylimidazole and Co²⁺ to 20: 1 (hereafter named as ZIF-Co-R/Cu; Fig. 1b and Supplementary Fig. S1). The ZIF-Co-R/Cu was converted into Cu–Co binary metal sulfides following a previously reported electrochemically conversion of MOF (EC-MOF) strategy^{65–67}. Upon adding 0.05 M Na₂HPO₄ as structure-tuning agents, the nanorod contour of ZIF-Co-R could be retained during the EC-MOF (Fig. 1c), which was otherwise changed into super-thin nanosheets (Supplementary Fig. S2). We denoted the PO₄³⁻-modified Cu–Co binary metal sulfides as CuCoSP_{no} and their products after further electrochemical redox activation as CuCoSP. This unique nanorod array configuration of CuCoSP can provide a more efficient pathway for mass and charge transport during the NO₃RR, contributing to the best performance of CuCoSP for NO₃RR as discussed below.

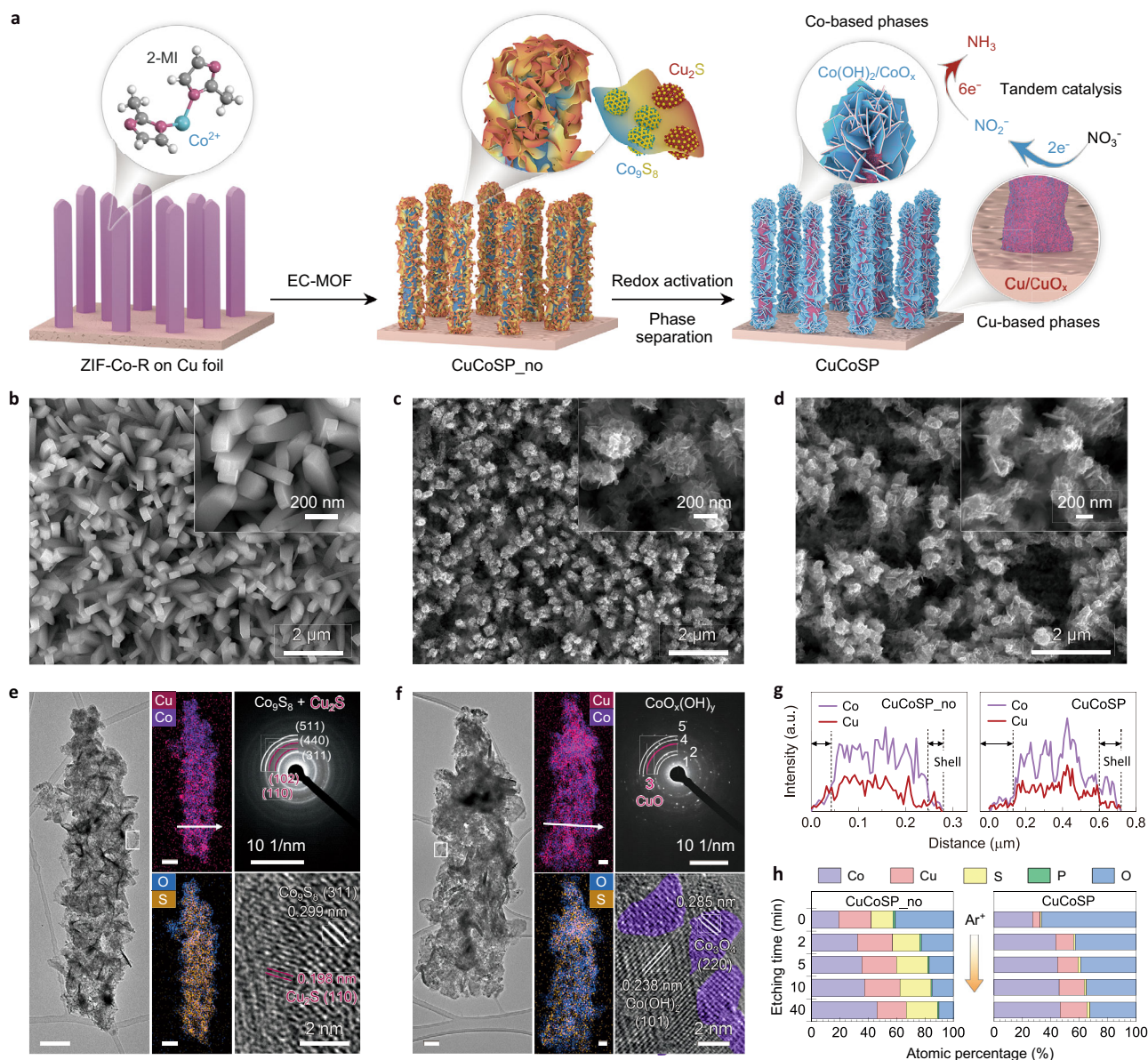


Fig. 1 Structural characterizations of catalysts. **a** Schematic illustration of the preparation of a Cu/Co-based binary 'tandem catalyst'. SEM images of the ZIF-Co-R precursor (**b**), CuCoSP_{no} (**c**) and CuCoSP (**d**) on the Cu foil substrate. The inset figures are the SEM images at higher magnification. **e, f** Typical TEM image, EDX mappings, SAED patterns and HR-TEM image of CuCoSP_{no} (**e**) and CuCoSP (**f**). Unlabelled scale bars are 100 nm. The SAED patterns in (**f**) show the presence of CuO phases and Co-based oxides/hydroxides (CoO_x(OH)_y), where 1 = Co(OH)₂ (100), 2 = Co(OH)₂ (101), 3 = CuO (202), 4 = CoOOH (211) and 5 = CoO (220). The purple colours of the HR-TEM image in (**f**) are marked to guide the eye and correspond to the Co₃O₄ nanocrystals. **g** EDX line-scan of a selected area marked by the white arrows in (**e**) and (**f**). **h** XPS-determined atomic percentage-depth profile of CuCoSP_{no} and CuCoSP as a function of Ar⁺ etching time. 2-MI 2-methylimidazole; EC-MOF electrochemically conversion of metal-organic frameworks.

Low-resolution transmission electron microscopy (TEM) and high-resolution scanning electron microscopy (HR-SEM) images reveal that a curly nanosheet-assembled shell wraps the nanorod skeleton of CuCoSP_{no} (Fig. 1c, e and Supplementary Fig. S3a). The corresponding EDX mapping shows strong Co, Cu and S signals well-distributed in the whole nanorod and a weak signal of O due to surface oxidation. Remarkably, Cu is also spread over the nanorod, indicating that the Cu comprised in CuCoSP_{no} is from the dissolution of Cu foil followed by redeposition and inward diffusion of the released Cu ions during the EC-MOF. The enrichment of Cu on the CuCoSP_{no} surface is supported by the EDX-linear scan (Fig. 1g and Supplementary Fig. S3). Moreover, HR-TEM images, coupled with selected area electron diffraction (SAED), reveal that the curly nanosheets and skeleton of

CuCoSP_{no} are mainly composed of ~3–5 nm Co₉S₈ and Cu₂S nanocrystals, which are not detectable by X-ray diffraction (XRD) (Supplementary Fig. S4d)^{59,66}.

After the electrochemical activation, the obtained CuCoSP preserves the contour of CuCoSP_{no}, except for the in situ formation of a hexagon-shaped nanosheet-assembled shell (Fig. 1d, f and Supplementary Fig. S5a). Compared to CuCoSP_{no}, the CuCoSP possesses more complex SAED patterns corresponding to multiple mixed phases (Fig. 1f), which include Co(OH)₂, CoOOH, CoO and CuO EDX mappings and linear EDX scans (Fig. 1f and Supplementary Fig. S5f) show weaker S and enhanced O signals. These results suggest a significant transformation of Cu–Co binary sulfides into oxides and hydroxides, as corroborated by the XRD patterns

(Supplementary Fig. S4e), as well as Raman and X-ray photoelectron spectroscopy (XPS). An HR-TEM image of a hexagon-shaped nanosheet on CuCoSP shows a typical (101) facet of $\text{Co}(\text{OH})_2$ and some Co_3O_4 nanocrystals at the edge. The EDX mapping of CuCoSP shows an intertwined distribution of Cu and Co on the nanorod (Fig. 1f), and the linear EDX scan reveals a higher content of Co in the shell region (Fig. 1g). Therefore, the shell assembled by xagon-shaped nanosheets is a Co element-rich phase, and the redox activation might induce the redistribution of Co-based and Cu-based phases.

To investigate the spatial arrangement of Cu-based and Co-based phases, we carried out XPS depth profiling. We calculated the atomic percentages of Cu, Co, O, S and P in both CuCoSP_no and CuCoSP as a function of Ar^+ etching time (Fig. 1h and Supplementary Fig. S6). We found that the CuCoSP_no has a Cu-rich surface (Co: Cu = 0.862: 1) and Co-rich core (Co: Cu = 1.83: 1 at 40 min etching time), which is in line with the EDX-linear scan results. The surface of CuCoSP is enriched with Co with a Co/Cu ratio of 5.23: 1. After 5 min etching time, the Co/Cu ratio decreases to 3.07: 1 and slightly decreases in the following 35 min of Ar^+ etching. The results reveal an electrochemical redox activation-induced outward diffusion of Co ions and a relative inward diffusion of Cu ions, contributing to the phase separation in CuCoSP. The outward diffusion of Co ions is attributed to the easier oxidation of cobalt sulfides than copper sulfides into corresponding oxides or hydroxides. EDX mapping images of CuCoSP_no after one-cycle redox activation provide further evidence (Supplementary Fig. S7), with the maps of Co and O overlapping on the outer-shell layer and those of Cu and residual S in the inner-core layer. This controllable phase separation in metal sulfide matrix driven by electrochemically redox activation may offer a strategy for a tandem catalyst design, which enables in situ formation of multiple active phases and rich phase interfaces for rapid spillover and transfer of reaction intermediates.

This core-shell arrangement of the Cu-based phases and Co-based phases, together with the rich phase interface between them, is the key to achieve a near-unity selectivity for subsequent NO_3^- -to- NH_3 catalysis on CuCoSP. The Cu foil substrate of CuCoSP may play a similar role to the Cu-based phases (Fig. 1a). As a control, we used a Cu foil or ZIF-Co-R grown on carbon paper (CC) as precursors and treated them by the same EC-MOF and activation procedures (Supplementary Fig. S8). The related materials were denoted as CuSP and CoSP, respectively.

NO_3RR performance. Linear sweep voltammetry (LSV) and one-hour electrolysis were performed for assessing the activity and selectivity of the as-synthesized catalysts in 0.01 M KNO_3 and 0.1 M KOH (pH 13) (Fig. 2a–c). Unless otherwise noted, all potentials are corrected vs the reversible hydrogen electrode (RHE). Performing NO_3RR in alkaline media was chosen due to the reported lower probability of the formation of toxic intermediates in solution (e.g., nitrogen oxides and NH_2OH), as compared to those in acidic or neutral media, as well as the need of removing NO_3^- ions in alkaline nuclear wastewater^{21,42}. We set the concentration of nitrate to be 0.01 M, which ensures the concentration of formed NH_3 to be easily higher than that of environmental contaminants which in turn helps to compare the intrinsic activity of the catalysts via bypassing the positive effects of high-concentration NO_3^- (e.g., 1 M) with respect to facilitating the NO_3RR ^{52,68}.

The LSV of CuSP in the presence of NO_3^- is similar to that of the NO_3RR on the Cu (100) facet⁴², where a diffusion-limited maximum total current density (j_{total}) of -55.3 mA/cm^2 is reached at around -0.3 V . At $< -0.3 \text{ V}$, the surface of CuSP becomes blocked by the strongly adsorbed intermediates of the

H_2 evolution reaction (HER) and/or NO_3RR until the surface is renewed because of the drastic HER at $< -0.6 \text{ V}$ ⁴². CoSP requires a $\sim 150 \text{ mV}$ more negative potential to drive the NO_3RR , but it shows a sharply increased j_{total} for the HER at $< -0.2 \text{ V}$, where metallic Co is supposedly formed (Supplementary Fig. S9). The CuCoSP has the catalytic features of both CuSP and CoSP, showing the highest NO_3RR activity between -0.16 V and 0.085 V . Moreover, the Tafel slope of CuCoSP for the HER in 0.1 M KOH is 69 mV dec^{-1} , and smaller than those of CuSP (125 mV dec^{-1}) and CoSP (104 mV dec^{-1}), suggesting faster kinetics for the HER (Supplementary Fig. S9). Thus, there is a strong synergy between the Cu-based and Co-based phases in CuCoSP for NO_3RR at $> -0.2 \text{ V}$ and HER at $< -0.2 \text{ V}$.

Determination of the product selectivity for CuSP, CoSP and CuCoSP shows a significant difference in the FE for NH_3 and NO_2^- (Fig. 2b, c and Supplementary Figs. S10–13). At low overpotentials ($> -0.2 \text{ V}$), CuSP exclusively catalyzes the formation of NO_2^- , while CoSP shows a high inherent NH_3 selectivity without any interference from the underlying CC (Supplementary Fig. S14d). The CuCoSP inherits the advantages of CoSP and reaches a maximum FE of 95.9% for NH_3 at -0.075 V , 14.5% higher than that of CoSP. This finding further suggests the synergy of the Cu-based and Co-based phases in CuCoSP for selective NO_3^- -to- NH_3 conversion. Moreover, the CuCoSP shows a FE of 88.7% for NH_3 and an NH_3 partial current densities (j_{NH_3}) of -9.54 mA cm^{-2} at -0.025 V , a potential at which CuSP exhibits exclusive NO_2^- generation and CoSP shows a negligible NO_3RR activity (Fig. 2a–d and Supplementary Figs. S11–13). CuCoSP retains this advantage even at 0.025 V (a FE of 66.4% for NH_3 and a j_{NH_3} of -3.84 mA cm^{-2}). Similar to CuSP, the Cu foil and inner Cu-based phases of CuCoSP can catalyze the preferential formation of NO_2^- , which might then be further reduced to NH_3 at the outer Co-based phases. This hypothesis, as further demonstrated below, may well account for the ~ 2 -fold higher j_{NH_3} for CuCoSP than that of CoSP at $> -0.175 \text{ V}$ (Fig. 2d).

At higher overpotentials ($< -0.2 \text{ V}$), CuCoSP and CoSP show a sharp decline of the FE for NH_3 but minor changes in their FE for NO_2^- ($< 1\%$) (Fig. 2b–d), indicating that the NO_3RR on CuCoSP and CoSP is challenged by the drastically enhanced HER (Supplementary Fig. S9). The competing HER was previously suppressed by increasing the NO_3^- concentrations and/or the pH value of electrolytes^{45,52}. As anticipated, j_{total} of CuCoSP linearly increases with the NO_3^- concentrations (Supplementary Fig. S15), indicative of a first-order reaction kinetics. At -0.175 V , the CuCoSP catalyst reaches a nearly equal FE of $93.3 \pm 2.1\%$ for NH_3 and a linearly increased NH_3 yield rate (Y_{NH_3}) with a value of 15.7, 33.4, 74.1, 155 and $327 \mu\text{mol h}^{-1} \text{ cm}^{-2}$ in 1, 2, 5, 10 and 20 mM NO_3^- , respectively (Fig. 2e). When the NO_3^- concentration increases to 50 and 100 mM, the Y_{NH_3} of CuCoSP reaches 0.690 and $1.17 \text{ mmol h}^{-1} \text{ cm}^{-2}$, respectively. The latter is comparable to the highest reported value of $1.17 \text{ mmol h}^{-1} \text{ cm}^{-2}$ on strained Ru nanoclusters evaluated at -0.2 V in 1 M NO_3^- and 1 M KOH (pH 14)⁵². The turnover numbers (TON) of nitrate on CuCoSP, defined by the ratio of the yielded NH_3 concentration $[\text{NH}_3]$ to the converted NO_3^- concentration $[\text{NO}_3^-]$, are close to 1 at $[\text{NO}_3^-] < 20 \text{ mM}$. This indicates that the formed NH_3 is mainly derived from the NO_3^- electroreduction rather than any environmental contaminations (Fig. 2e and Supplementary Fig. S15d). However, the TON value decreases to ~ 0.8 in 100 mM nitrate electrolytes, suggesting that high $[\text{NO}_3^-]$ might induce the formation of gaseous by-products (e.g., N_2 and NO_x)³⁶. Finally, the CuCoSP achieves a half-cell energy efficiency of NH_3 (EE_{NH_3}) close to 40%. These results endow the proposed CuCoSP ranking among the best NH_3 synthesizing electrocatalysts (Supplementary Table S1).

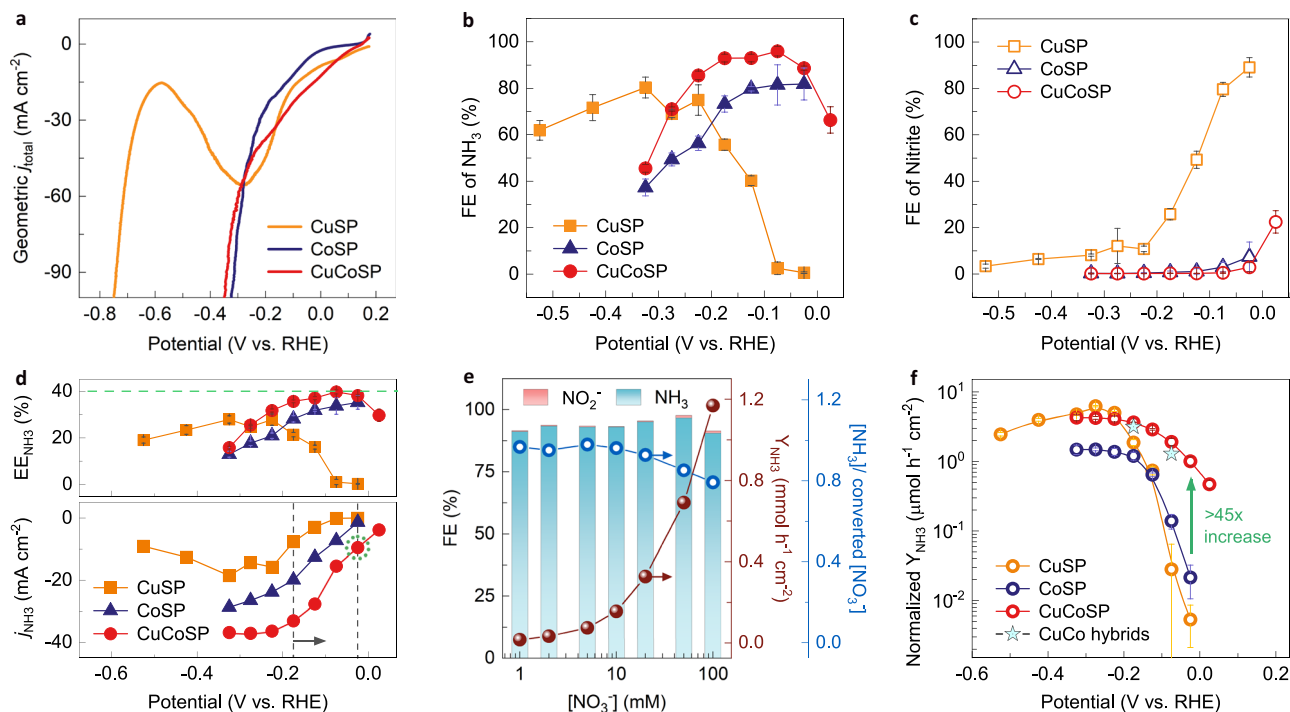


Fig. 2 NO_3^- -to- NH_3 conversion performance. LSVs at a scan rate of 5 mV s^{-1} (a), Faradaic efficiencies (FE) for NH_3 (b) and NO_2^- (c) on CuSP, CoSP and CuCoSP in 0.01 M NO_3^- and 0.1 M KOH (pH 13) at various applied potentials. d A comparison of half-cell energy efficiencies of NH_3 (EE_{NH_3}) and partial current densities of NH_3 (j_{NH_3}) on CuSP, CoSP and CuCoSP catalysts at various potentials. e The FE of NO_2^- and NH_3 , the NH_3 yield rate (Y_{NH_3}), as well as the ratio of the formed NH_3 concentration $[\text{NH}_3]$ to the converted NO_3^- concentration $[\text{NO}_3^-]$ on the CuCoSP catalyst at -0.175 V vs. RHE at $[\text{NO}_3^-]$ in the range of 1–100 mM at pH 13. f The ECSA-normalized Y_{NH_3} on CuSP, CoSP, CuCoSP and metallic CuCo hybrids in 0.01 M NO_3^- and 0.1 M KOH at various potentials. Error bars denote the standard deviations calculated from three independent measurements.

To assess the origin of the detected NH_3 and correct the Y_{NH_3} , we employed ^1H NMR to detect the NH_3 generation on CuCoSP in 0.1 M KOH containing $0.01 \text{ M } ^{15}\text{N}$ -labelled $^{15}\text{NO}_3^-$ or $^{14}\text{NO}_3^-$ (Supplementary Fig. S16). The $^{14}\text{NH}_3$ yield quantified by ^1H NMR is very close to that determined by colorimetric methods⁶⁹, confirming the reliability of our results. The negligible NH_3 generation in blank 0.1 M KOH and the typical ^1H NMR double peaks of $^{15}\text{NH}_4^+$ after the electrolysis of $^{15}\text{NO}_3^-$ suggest that the obtained NH_3 indeed originates from the NO_3RR ^{25,28,44}.

To derive the intrinsic activities of the catalysts, we normalize their Y_{NH_3} by the electrochemical active surface area (ECSA) (correlated with the double-layer capacity (C_{dl})) (Fig. 2f and Supplementary Fig. S17). At low overpotentials, the Y_{NH_3} of CuCoSP can be ~ 45 times and two orders of magnitude higher than those of CoSP and CuSP, respectively, confirming the high intrinsic performance of CuCoSP. Remarkably, CuSP lost activity rapidly at $> -0.525 \text{ V}$ during the NO_3^- electrolysis (Supplementary Fig. S11), which occurred neither at CoSP nor at CuCoSP (Supplementary Fig. S12 and S13). This finding indicates that the Co-based phases existing in CoSP and CuCoSP may help to avoid similar poisoning effects. When the NO_3RR was performed at -0.175 V for 10 h over the CuCoSP catalyst, no appreciable decay in activity and selectivity for NO_3^- -to- NH_3 conversion was observed, and the structural features of CuCoSP were retained (Supplementary Fig. S18).

Understanding the high-rate NH_3 generation on CuCoSP.

Electrocatalytic NO_3RR follows a consecutive pathway (Fig. 3a), where NO_2^- is generated as a stable intermediate^{17,36}. A fast NO_3^- -to- NH_3 conversion requires the simultaneous acceleration of the sequential NO_3^- -to- NO_2^- and NO_2^- -to- NH_3 reactions^{35,36}. To rationalize the high Y_{NH_3} on CuCoSP at low overpotentials, we

firstly compared the potentials of the three catalysts required to reach -1 mA cm^{-2} (kinetic area with negligible mass transport limitation) in 0.01 M NO_3^- and NO_2^- , respectively (Supplementary Fig. S20). CuSP shows a 176 mV more positive potential than CoSP for NO_3^- reduction, while CoSP has a 251 mV more positive potential than CuSP for NO_2^- reduction. Therefore, CuSP and CoSP may play a complementary role for the consecutive NO_3RR . Significantly, CuCoSP combines the positive properties of CuSP and CoSP for NO_3^- and NO_2^- reduction, respectively, implying that there are likely two types of active phases in CuCoSP: Cu-based phases which are similar to those in CuSP, and Co-based phases which are similar to those in CoSP. The two types of active phases in CuCoSP synergistically catalyze the tandem NO_3RR .

To validate this hypothesis, we further evaluated the rate constants k_1 and k_2 of each catalyst for NO_3^- -to- NO_2^- and NO_2^- -to- NH_3 conversion, respectively (Supplementary Fig. S21 and Table S2). We found that the rate constants of the three catalysts follow a similar trend as their potentials at -1 mA cm^{-2} ; a larger rate constant corresponding to a more positive potential for reaching -1 mA cm^{-2} (Fig. 3a). The largest k_1 but the smallest k_2 values of CuSP correspond to a fast reduction of NO_3^- to NO_2^- and subsequent desorption of NO_2^- to the electrolyte, resulting in the observed high FE of NO_2^- (Fig. 2c and Supplementary Fig. S11). On the CuCoSP surface, NO_2^- intermediates are preferentially formed on Cu-based phases and then split over to nearby Co-based phases. Compared to the k_2/k_1 ratio of CuSP (0.468), the larger k_2/k_1 ratios of CoSP (3.14) and CuCoSP (1.78) suggest a fast reduction of the intermediate NO_2^- to NH_3 over their Co-based phases, thus well explaining their near-unity selectivity for NH_3 generation. We used the k_1 values of CoSP and CuCoSP to estimate their local surface NO_2^- concentration during the NO_3RR and find a 1.54-fold higher value on CuCoSP than on CoSP (Supplementary Table S2), which

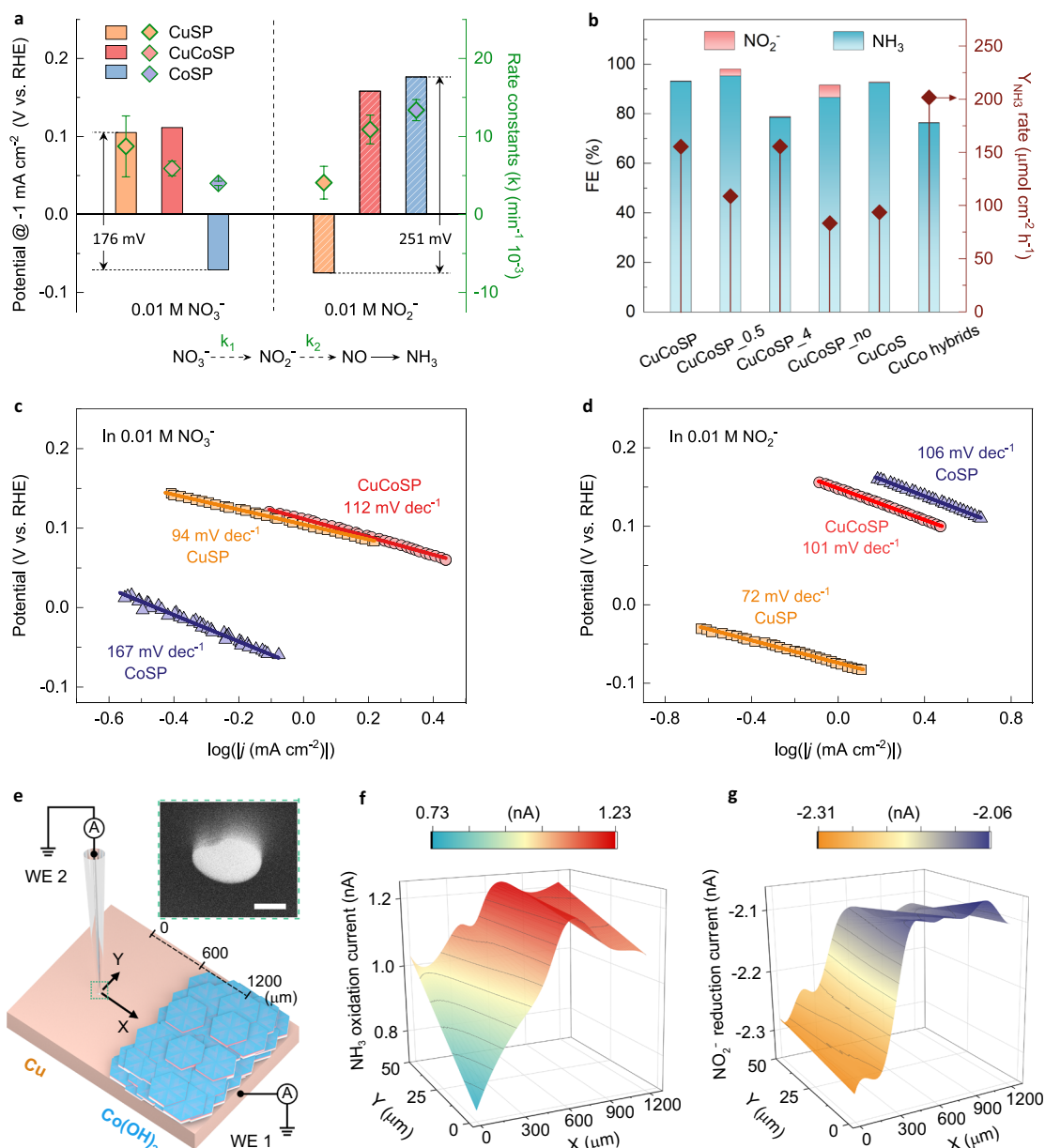


Fig. 3 Evaluation of the reaction kinetics and mechanisms of the catalysis of the NO_3RR . **a** The LSV-derived potentials at a current density of -1 mA cm^{-2} and the calculated reaction constants (k , k_1 for NO_3^- -to- NO_2^- and k_2 for NO_2^- -to- NO conversion) for NO_3^- and NO_2^- reduction on CuSP, CoSP and CuCoSP catalysts. k was calculated based on the concentration evolution of NO_3^- or NO_2^- ions as a function of electrolysis time at -0.175 V vs. RHE in 0.01 M NO_3^- and NO_2^- at pH 13. Error bars denote the standard deviations of k calculated at different time points during 1 h electrolysis. **b** A comparison of the FE and the Y_{NH_3} on the control catalysts: CuCoSP_0.5, CuCoSP_4, CuCoSP_no, CuCoS and metallic CuCo hybrids. The LSV-derived Tafel slopes of CuSP, CoSP and CuCoSP in 0.01 M nitrate (**c**) and nitrite (**d**) at pH 13, respectively. The LSVs were recorded at a scan rate of 1 mV s^{-1} . **e** Schematic representation of the SECM setup that is operated in a sample generation-tip collection (SG-TC) mode using a Pt-UME (WE 2) to detect NO_2^- and NH_3 produced during NO_3RR on Cu-Co(OH)_2 model catalyst (WE 1). Inset: SEM image of Pt-UME tip; scale bar is 500 nm . **f, g** Current maps of NH_3 oxidation (**f**) and NO_2^- reduction (**g**) recorded at 0.76 V and 0.06 V (vs. RHE) at the Pt-UME, respectively, when a potential of -0.12 V (vs. RHE) is applied to the Cu-Co(OH)_2 model catalyst in 50 mM NO_3^- at pH 13.

is consistent with the observed 1.66-fold larger j_{NH_3} of CuCoSP compared to CoSP at -0.175 V (Fig. 2d). This finding unveils the crucial role of Cu-based phases in CuCoSP for creating a high local NO_2^- concentration, which accelerates subsequent NH_3 generation on its Co-based phases, ultimately contributing to the tandem catalysis of NO_3RR .

Considering the lowest k_1 value of CoSP, the smaller k_1 value of CuCoSP than CuSP can be rationalized since the less active Co-based phases of CuCoSP may block its active Cu-based phases (especially the Cu foil substrate) for NO_3^- reduction. As such, we

synthesized the CuCoSP_0.5 and CuCoSP_4 with 0.5 h and 4 h growth of ZIF-Co-R on Cu foil, respectively. The CuCoSP_0.5 shows catalytic features close to CuSP, thus giving a higher FE for NO_2^- than CuCoSP (Fig. 3b and Supplementary Fig. S22). This finding indicates that possible Co doping in Cu-based phases of CuCoSP_0.5 does not change their catalytic nature. Likewise, the CuCoSP_4 shows a similar catalytic feature to CoSP with a low sum FE for NO_3RR . Therefore, the content ratio of Cu-based and Co-based phases in CuCoSP, rather than the Cu or Co doping, determines the rates of the NO_3^- -to- NO_2^-

and NO_2^- -to- NH_3 reactions. This is a typical feature of tandem catalysts^{39,59}.

Electrokinetic analysis was conducted to determine the rate-determining step (RDS) of the NO_3^- and NO_2^- reduction catalyzed by the three catalysts. In 0.01 M NO_3^- (Fig. 3c), CuSP and CuCoSP show Tafel slopes of 94 and 112 mV dec⁻¹, respectively, a little lower than 120 mV dec⁻¹, suggesting that the RDS is the first one-electron transfer occurring during the NO_3^- -to- NO_2^- conversion^{34,48,70}. The much higher Tafel slope of CoSP (167 mV dec⁻¹) indicates that the NO_3RR over CoSP is limited by the initial adsorption and activation of NO_3^- ⁴⁸. In 0.01 M NO_2^- (Fig. 3d), CoSP and CuCoSP show Tafel slopes of 106 and 101 mV dec⁻¹, respectively, suggesting that the RDS is the first one-electron transfer for the reduction of NO_2^- to NO ^{34,48}. CuSP has a Tafel slope of 72 mV dec⁻¹, close to the critical value of 60 mV dec⁻¹, implying that the RDS is a chemical step^{71,72}. Based on the theoretical NO_3RR pathways on Cu⁴⁴, this RDS is likely the coupling of strongly adsorbed *NO and *H. Remarkably, the smaller Tafel slope of CuSP than those of CoSP and CuCoSP points to a faster NO_2^- reduction kinetics on CuSP, but CuSP suffers from a faster deactivation in 0.01 M NO_2^- than in 0.01 M NO_3^- (Supplementary Fig. S21), thus giving the smallest apparent k_2 value. Accordingly, the observed poisoning of CuSP might be ascribed to the strongly adsorbed *NO species. Therefore, CuCoSP combines the nature of CuSP for NO_3^- reduction with that of CoSP for NO_2^- reduction.

To assess the possible roles of anionic ligands (PO_4^{3-} and S^{2-}) in our system, we tested the NO_3RR performance of CuCoSP_no catalysts with the maximum PO_4^{3-} and S^{2-} ligands and CuCoS catalysts with only S^{2-} ligand. The lower FE (for NH_3) and Y_{NH_3} of CuCoSP_no compared with those of CuCoSP (Fig. 3b), in combination with the near-unity NH_3 selectivity but low Y_{NH_3} of CuCoS (Fig. 3b and Supplementary Fig. S23), suggest that PO_4^{3-} and S^{2-} ligands most likely do not play a prominent role. We evaluated the final morphology of CuCoSP after repeating three electrolysis of one hour at -0.325 V and observed a separation of Cu-based phases (nanorods) and Co-based phases (hexagonal nanosheets) based on EDX mapping and HR-TEM images (Supplementary Fig. S24). This result rules out the formation of a bulk CuCo alloy, as corroborated by the XRD patterns (Supplementary Fig. S4f). To identify the impact of surface CuCo metallizing and/or alloying possibly during the NO_3RR , we electrodeposited a hybrid of Cu–Co metals and alloy (Co: Cu = 2.82: 1, close to that on CuCoSP surface) on CC (Supplementary Fig. S25). The metallic CuCo hybrids show Tafel slopes of 61 mV dec⁻¹ in 0.01 M NO_3^- and 79 mV dec⁻¹ in 0.01 M NO_2^- , indicating a significantly different catalytic mechanism and kinetics than CuCoSP. Despite its higher apparent Y_{NH_3} , the CuCo hybrids have a lower FE for NH_3 and ECSA-normalized Y_{NH_3} than CuCoSP (Fig. 2f and 3b). The ECSA-normalized Y_{NH_3} of CuCo hybrids is about 85 and 67% of that formed on CuCoSP at -0.175 V and -0.025 V, respectively. As such, the excellent intrinsic performance of CuCoSP towards NH_3 generation, especially at low overpotentials, is unlikely from surface Cu–Co metallizing or alloying. It can be concluded that the high-rate NO_3^- -to- NH_3 conversion on CuCoSP is due to the coexistence of the complementary Cu-based and Co-based phases: the former catalyzes NO_3^- -to- NO_2^- reduction and the latter catalyzes the NO_2^- -to- NH_3 conversion, contributing to the tandem catalysis of NO_3RR .

To offer a direct evidence for this tandem catalysis of NO_3RR , we performed SECM experiments in a surface-generation tip-collection mode, which involves using a positioned Pt ultramicroelectrode (Pt-UME) to detect the NO_2^- and NH_3 formed on the surface of a Cu₂Co(OH)₂ model catalyst (Fig. 3e) during the NO_3^- electrolysis. This Cu₂Co(OH)₂ model catalyst has two

adjacent layers to simulate the CuSP (Cu layer) and CoSP (Co(OH)₂ layer) catalysts, while the border between the two layers may play a similar role of as the adjacent phases in CuCoSP (Supplementary Fig. S26). During the SECM measurements, the catalyst layer was polarized to -0.12 V (vs. RHE), while at the positioned Pt-UME cyclic voltammetry (CV) in the potential range between -0.12 V and 1.58 V (vs. RHE) at a rate of 200 mV s⁻¹ was performed. We were applying -0.12 V at catalysts as we found that at this potential, CuSP and CoSP is relatively more stable and active compared to potentials of -0.075 V and -0.025 V, which is beneficial for in situ detection of the intermediately formed NO_2^- and NH_3 . The same reason is the use of a concentration of 50 mM NO_3^- . At -0.12 V, CuSP mainly produces NO_2^- , and CoSP exhibits a much lower NO_3RR activity compared to CuCoSP, as indicated in Fig. 2a–c and Supplementary Fig. S11–13.

We firstly performed cyclic voltammograms at the Pt-UME separately in 10 mM NO_3^- , NO_2^- and NH_4Cl at pH 13, which are compared with those in pure 0.1 M KOH (Supplementary Fig. S27a–c). The results indicate that the Pt-UME does not exhibit any activity for the NO_3RR , but it can efficiently catalyze NO_2^- reduction and NH_3 oxidation in alkaline media, which is well consistent with previous studies^{73–75}. This enables selectively detecting the in situ generated NO_2^- (at 0.06 V) and NH_3 (at 0.76 V) (Supplementary Fig. S27d–f), when the tip of Pt-UME approaches the surface of Cu₂Co(OH)₂ layer. Accordingly, a high current from NH_3 oxidation and NO_2^- reduction corresponds to a high local concentration of NH_3 and NO_2^- , respectively, above the surface of Cu₂Co(OH)₂ catalyst. The SECM array scans (Fig. 3f, g) reveal that the amount of generated NH_3 is substantially increasing at the border ($X \approx 600$ μm) between the Cu and Co(OH)₂ layers, accompanying by a sharply decreased amount of generated NO_2^- . The SECM results unequivocally confirmed that the NO_2^- is preferentially formed on the Cu layer and then diffuses to the near Co(OH)₂ layer, where the NO_2^- is reduced into NH_3 according to a typical tandem catalysis process. Note that the formed NH_3 at the border of the Cu₂Co(OH)₂ layers diffuses to both sides, leading to the formation of a concentration gradient around the border during the course of the SECM measurement.

Identification of the active phases for NO_3RR . Ex situ XPS and Raman spectra were obtained to identify the surface phase compositions of the three catalysts (Fig. 4, Supplementary Fig. S28 and Fig. S29). We find that the redox activation induced the transformation of the initial Cu/Co-based sulfide phases into the corresponding oxides and hydroxides (see detailed assignments of the XPS and Raman peaks in Supplementary Notes 1 and 2). As a result, CuSP consists of Cu⁰, CuO, Cu₂O and Cu(OH)₂^{53,54,76}, whereas CoSP is composed of Co²⁺-dominated CoO and Co(OH)₂, as well as Co³⁺-containing Co₃O₄ and CoOOH^{65,77–79}. As anticipated, CuCoSP exists as a combination of CuSP and CoSP in phase compositions, except for the observed suppression of Co³⁺-CoO_x phases and increase of Cu(OH)₂ phases (Fig. 4a, b), which points to the synergy interaction between Cu-based and Co-based phases in CuCoSP. O 1s XPS spectra reveal a ~2-fold higher content of O vacancies on CuSP and CuCoSP than on CoSP (Fig. 4c and Supplementary Fig. S28c)⁸⁰. Together with the observed smaller Tafel slopes of CuSP and CuCoSP compared to CoSP (Supplementary Fig. S28f), this result highlights a potential role of O vacancies in Cu-based phases for the initial adsorption and/or activation of free NO_3^- ions⁵⁰, which is a key challenge for most of the reported NO_3RR catalysts.

To derive the active phases for NO_3RR experimentally, we used in situ Raman spectroscopy to monitor the phase evolution of the

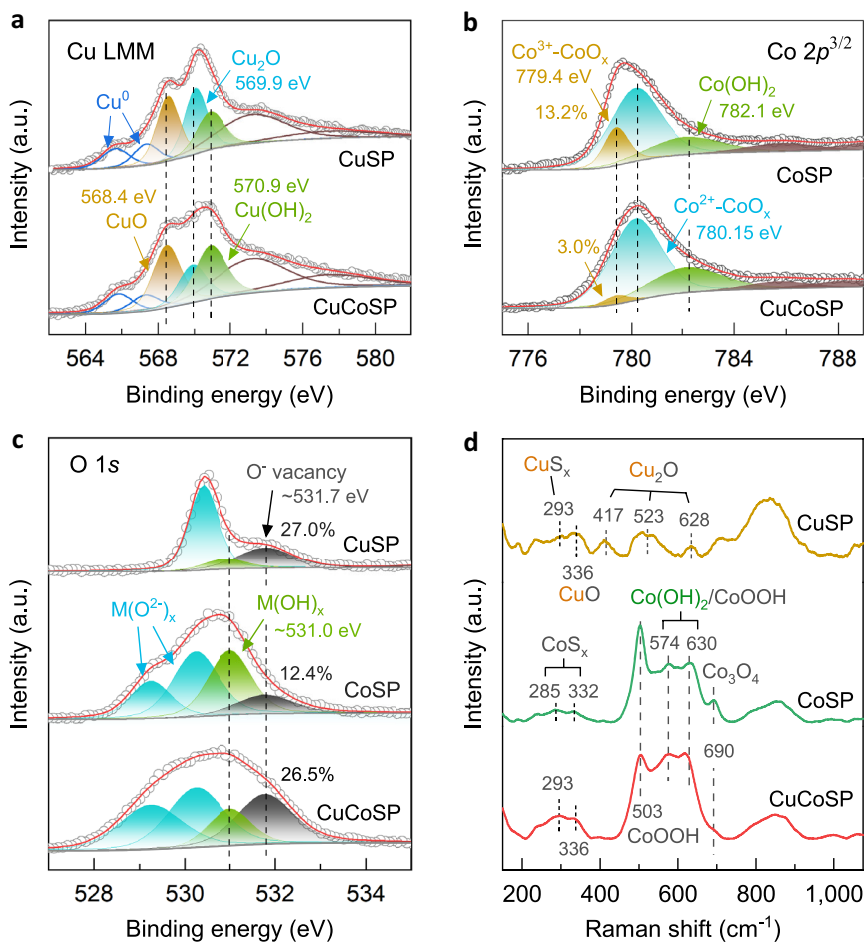


Fig. 4 Surface phase compositions of CuSP, CoSP and CuCoSP catalysts. Cu LMM (a), Co 2p^{3/2} (b) and O 1s (c) XPS spectra. d Ex situ Raman spectra.

three catalysts at a series of applied potentials in 0.01 M KOH in the presence or absence of 0.01 M NO₃⁻ (Fig. 5 and Supplementary Fig. S30). NO₃⁻ ions exhibit a characteristic peak at ~1050 cm⁻¹⁸¹. K₂SO₄ was added to ensure sufficient ionic conductivity and provides SO₄²⁻ ions as an external Raman reference with a typical signal at ~982 cm⁻¹⁵³.

Figure 5a shows the Raman spectra of CuSP at reducing potentials related to NO₃RR. The initial broad bands at 417, 523 and 628 cm⁻¹, associated with Cu₂O phases^{53,54}, persist at as low as -0.525 V. Remarkably, at <-0.175 V, two sets of peaks emerge at 341, 407, 491 and 524 cm⁻¹, previously assigned to Cu-O and Cu-OH modes, respectively⁵³. The same but more notable signals are observed in the absence of NO₃⁻ (Supplementary Fig. S30a), partly due to the NO₃RR delaying the surface phase evolution. It is worth noting that CuSP can prevent poisoning only at <-0.425 V, where the surface evolution of CuSP might promote stable NH₃ generation. As a control, we further assessed the performance of a metallic Cu foil for NO₃RR (Supplementary Fig. S14). The results show that at potentials >-0.425 V, Cu foil suffered from deactivation in a much higher rate, compared to CuSP containing mixed Cu/CuO_x phases. Moreover, at low overpotentials, the Cu foil mainly electrochemically catalyzes the reduction of NO₃⁻ to highly oxidative NO₂ and acts as reducing reagents for the subsequent chemical reduction of NO₂ to NO₂⁻, which is supported by the over 100% FE for NO₃RR at -0.025 and -0.125 V (vs. RHE) (Supplementary Fig. S14c). This chemical step will lead to the partial oxidation of metallic Cu to CuO_x in alkaline electrolytes. According to recent DFT calculations on Cu and mixed Cu/Cu₂O phase, the latter was suggested

to be more active for NO₃⁻ to NO₂⁻ conversion⁴⁴. Therefore, at low overpotentials, the catalytic nature of CuSP for NO₃RR is related to the Cu/CuO_x phases, considering the XPS-evidenced presence of Cu⁰ phase.

On the CoSP catalysts, the characteristic Raman peaks of multiple Co³⁺-based phases and Co(OH)₂ are fast attenuated with decreasing potentials from 0.025 V to -0.325 V (Supplementary Fig. S30b)⁷⁷⁻⁷⁹. This indicates the gradual conversion of Co³⁺-based phases and Co(OH)₂ into CoO and metallic Co in the absence of NO₃⁻⁷⁷. In 0.01 M NO₃⁻ the attenuation rate of these Raman peaks was much slower (Fig. 5b). Remarkably, the Raman signals associated with CoOOH and Co₃O₄ phases increase at 0.025 and -0.025 V, suggesting the partial oxidation of Co²⁺ in CoSP to Co³⁺^{77,78}. Because of this, the electrolysis product of NO₃⁻ at 0.025 and -0.025 V should be only the highly oxidative NO₂ species in Ar-saturated alkaline electrolytes⁴⁹, and their formation slows down the phase conversion. In this context, the Co²⁺-based phases act as chemical reducing reagents and offer additional electrons for reduction of NO₂ to NO₂⁻, after which the formed NO₂⁻ will be electrochemically reduced to NH₃ as evidenced by the low overpotential of CoSP for the NO₂⁻ reduction (Fig. 3a), finally contributing to the apparently highest FE for NH₃ at low overpotentials (Fig. 2b). At <-0.025 V, the Raman signals of Co³⁺-based phases and Co(OH)₂ start to weaken. This result, together with the potential at -1 mA cm⁻² of CoSP catalysts for NO₃⁻ reduction (-0.071 V), suggests that the fast reduction of NO₃⁻ into NO₂⁻ on CoSP requires the in-situ formation of metallic Co. By contrast, we found that the Co²⁺ in CoSP was

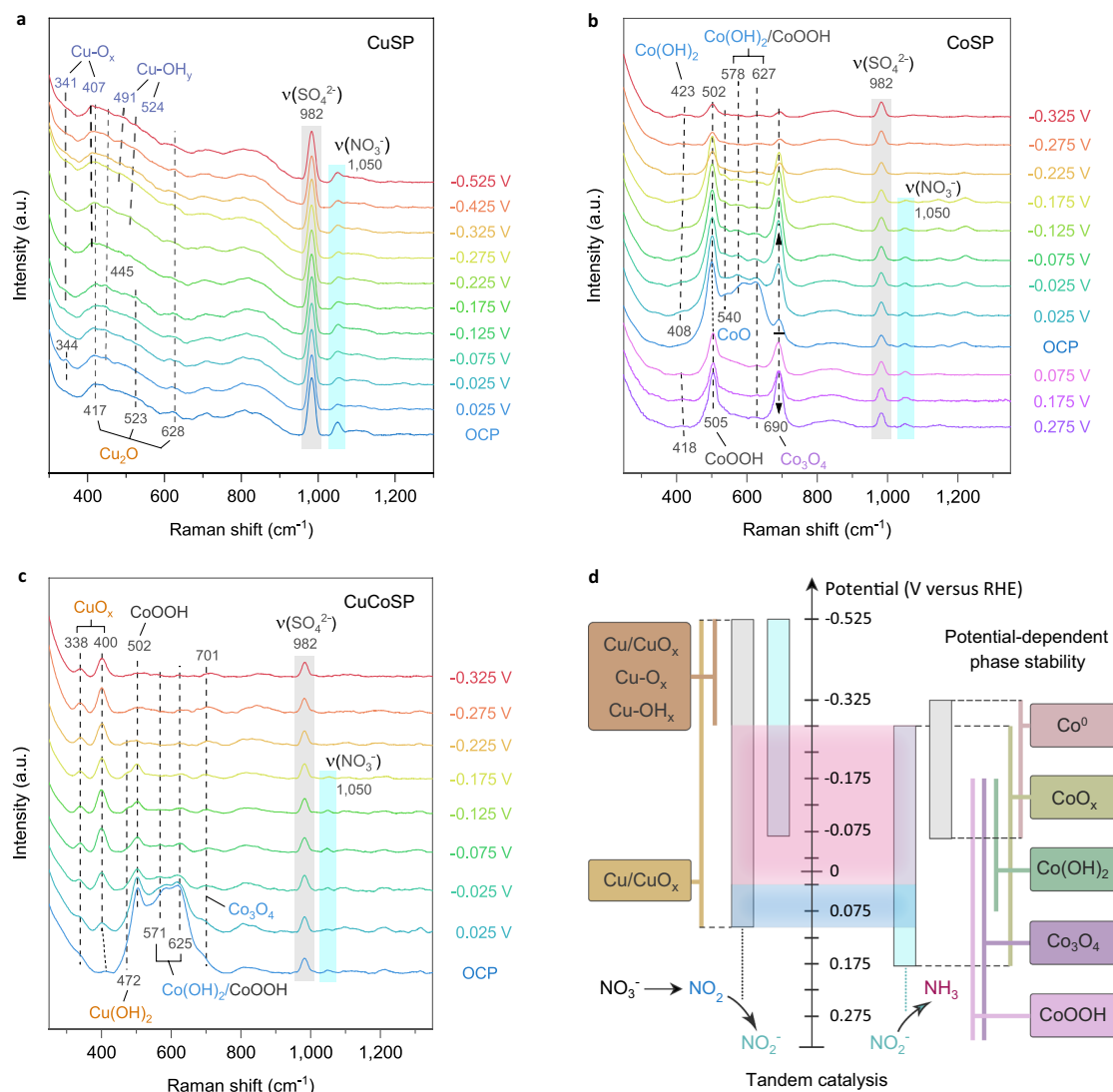


Fig. 5 In situ Raman spectra of the catalysts and schematic of the tandem mechanisms of CuCoSP catalysts. In situ Raman spectra of CuSP (**a**), CoSP (**b**) and CuCoSP (**c**) at different applied potentials in electrolytes containing 0.01 M NO₃⁻, 0.04 M K₂SO₄ and 0.01 M KOH. **d** A proposed reaction mechanism of CuCoSP tandem catalysis of NO₃⁻RR at low overpotentials. In the middle of (**d**), the light blue region corresponds to the potential range for the reduction of NO₃⁻ to NO₂ species at the Cu/CuO_x phases, resulting in the etching of catalysts, while the light pink region shows the potential range for efficient tandem reduction of NO₃⁻ to NH₃.

oxidized to Co³⁺ already at >0.025 V^{77–79}. Since the potential at -1 mA cm^{-2} of CoSP for NO₂⁻ reduction is limited to 0.176 V (Fig. 3a), it can be concluded that the sharply increased Co³⁺-based phases at potentials >0.025 V are inactive for NO₂⁻ reduction. Thus, the active phase of CoSP for reducing NO₃⁻ to NO₂⁻ is related to metallic Co, while that for NO₂⁻-to-NH₃ conversion is a Co²⁺-dominated CoO_x phase.

For CuCoSP, the Raman peaks associated with Co-based phases were quickly attenuated with decreasing potentials, while a phase assigned to CuO_x emerges at 338 and 400 cm^{-1} (Fig. 5c and Supplementary Fig. S30c)⁵⁴. These results suggest an electrochemically driven phase separation in CuCoSP, leading to the formation of hybrid of Cu/CuO_x and Co/CoO phases. The CuO_x persists to potentials as low as -0.325 V , further decreasing the probability of in situ surface CuCo alloying, especially at potentials $>-0.2 \text{ V}$. This is further supported by the XRD patterns, HR-TEM and EDX-mapping images of CuCoSP after repeating three electrolysis cycles of one hour at -0.325 V (Supplementary Fig. S4f and Fig. S24). The rate at which these Raman peaks are evolving is almost not impacted by the NO₃RR

(Fig. 5c and Supplementary Fig. S30c). This might be attributed to the high rate of NO₃RR on CuCoSP, which establishes a depletion layer of NO₃⁻ explaining the minor effects of the NO₃RR on the phase-evolving rate. In stark contrast to CoSP (Fig. 5b), the Raman signals of Co³⁺-based phases in CuCoSP were not enhanced at both 0.025 and -0.025 V in 0.01 M NO₃⁻. This finding indicates fast reduction of NO₃⁻ to NO₂⁻ rather than to oxidative NO₂ species on the Cu-based phases of CuCoSP. Accordingly, the active Co²⁺-based phases of CuCoSP are stabilized by the Cu/CuO_x phases, both of which are combined to form a tandem system for cascade NO₃⁻-to-NH₃ conversion at low overpotentials (Fig. 5d).

Discussion

In summary, we present a concept for designing efficient tandem catalysts, which involves the coupling of potential-dependent intermediate phases of transition metals to act as cooperative catalytic sites for cascade NO₃⁻-to-NH₃ conversion. This concept was verified using Cu/CuO_x-Co/CoO hybrids with a well-defined

spatial arrangement that is achieved by electrochemical redox activation-induced phase reconstruction of Cu/Co-based binary metal sulfides. In this tandem catalysis system, NO_3^- ions are reduced to NO_2^- preferentially on Cu/CuO_x phases, while the NO_2^- intermediates are then transferred and selectively converted to NH_3 on Co/CoO phases. The sequential NO_3^- and NO_2^- reduction on two different adjacent metal/metal oxide phases enables a high-rate NH_3 generation at low overpotentials. At -0.175 V vs. RHE, the designed CuCoSP catalysts show an excellent FE for NH_3 (90.6%) and super-high Y_{NH_3} of 1.17 mmol cm^{-2} h^{-1} in 0.1 M NO_3^- at pH 13, outperforming most of the NO_3RR catalysts at the same conditions. Although tandem catalysis was widely employed in heterogeneous systems, this study provides a direct demonstration of efficiently using distinct potential-dependent intermediate phases as tandem catalytic sites. This concept of splicing active phases of transition metals represents a powerful strategy towards designing high-performance, multi-functional electrocatalysts for multi-step chemical reactions, such as e.g. urea electrosynthesis by integrating NO_3RR with CO_2 reduction.

Methods

Chemicals. Na_2HPO_4 ($\geq 99.0\%$) and NaClO solution (17%) were purchased from VWR. Maleic acid ($\geq 99.0\%$) was obtained from Riedel-de Haën. All other chemicals and Cu foil (99.98%) were from Sigma-Aldrich. All chemicals were used without further purification. Carbon cloth was provided by PHYCHEMI.

Growth of ZIF-Co-R nanorods on Cu foil and carbon cloth. The Cu foil (3×0.5 cm^2) was washed with acetone, ethanol and distilled water, finally dried by blotting paper before use. The CC was initially treated with 1 M HCl ($\geq 37\%$) for 12 h, washed with deionized water and dried in a 70°C oven. Then, the CC was soaked in an aqueous solution of 2-methylimidazole (0.4 M, 99% purity) for 12 h and dried by blotting paper before use. For the growth Co-ZIF-R nanorods, the Cu foil or CC was immersed into a 14 ml growth solution, which was prepared by adding 10 ml of 2-methylimidazole (0.4 M) into 4 ml aqueous solution of $\text{Co}(\text{NO}_3)_2 \cdot 6\text{H}_2\text{O}$ (50 mM, $\geq 98\%$). The Co-ZIF-R nanorods were grown under static conditions at 25°C for 105 min. The purple Co-ZIF-R nanorods on Cu foil or CC were washed with deionized water and dried in a 70°C oven.

EC-MOF for synthesis of CuCoSP_{no}. In a typical three-electrode system, the Co-ZIF-R on Cu foil was used as the working electrode, and Ag/AgCl (sat. KCl) and an FTO slide were employed as the reference and counter electrodes, respectively. In Ar-saturated electrolytes (aqueous solution of 0.5 M thiourea ($\geq 99.0\%$), 0.25 M KCl ($\geq 99.0\%$) and 0.05 M Na_2HPO_4), the ZIF-Co-R was electrochemically converted via continuous CV scanning between -1.76 V and -0.15 V at a series of scan rates for different CV cycles (at 0.2 V s^{-1} for 1200 CV cycles, at 0.1 V s^{-1} for 300 CV cycles, at 0.05 V s^{-1} for 150 CV cycles and finally at 0.02 V s^{-1} for 100 CV cycles) using an Autolab potentiostat. The black products on Cu foil were taken out, rinsed with water and acetone, blow-dried by Ar gas and stored at -21°C for further characterization. Using the same method, the CuSP_{no} was prepared from Cu foil directly; the CoSP_{no} on CC was synthesized using ZIF-Co-R nanorods on CC as precursors; the CuCoS_{no} on Cu foil was obtained in an electrolyte with no Na_2HPO_4 . As a control, metallic CuCo hybrids were prepared via electrodeposition of CuCo metals and alloy on CC in 0.05 M H_2SO_4 (98%) solution containing 4 mM CuSO_4 ($\geq 99\%$) and 16 mM CoSO_4 ($\geq 99\%$) at -1.75 V vs. Ag/AgCl for 400 s.

Electrochemical redox activation of the samples. Using a Gamry interface 1000 workstation, the samples were activated in 0.1 M KOH ($\geq 85\%$) and 0.01 M potassium nitrate ($\geq 99\%$) at 60 mA cm^{-2} for 45 s. They then underwent continuous LSV sweeping at a rate of 20 mV s^{-1} from -0.8 V to -1.65 V (vs. Ag/AgCl) until the polarization curves reached a steady state. This activation process was repeated two or three times. Then, the samples were gently washed with water and acetone, and dried under Ar flow for further tests or characterizations. After the redox activation, the samples of CuCoSP_{no}, CuSP_{no}, CoSP_{no} and CuCoS_{no} were named as CuCoSP, CuSP, CoSP and CuCoS, respectively.

Material characterization. SEM was performed using a Quanta 3D FEG scanning electron microscope. TEM images, high-angle annular dark-field TEM images, SAED patterns, element mappings and EDX line-scan were carried out on a JEOL-2800 TEM/STEM system using gold grids. XPS was recorded using an AXIS Nova spectrometer (Kratos Analytical) equipped with a monochromatic Al K α X-ray source (1487 eV, 15 mA emission current) and an inert ion gas gun for depth-profiling composition analysis as a function of etching time. For the core-level spectra, the binding energies were calibrated based on the C 1s feature located at

284.8 eV. The nuclear magnetic resonance (NMR) spectroscopy was performed on a Bruker 400 MHz NMR spectrometer. XRD were obtained using a Bruker D8 Discover X-ray diffractometer with Cu K α radiation ($\lambda = 1.5418\text{\AA}$).

Electrochemical NO_3RR tests. The electrochemical tests were performed using a three-electrode system connected to the Gamry workstation in a typical H-type cell. The H-type cell was separated by a Nafion 117 membrane (Dupont) that was pretreated following reported procedures⁸². The catalysts were used as the working electrode, while Ag/AgCl (3 M KCl) and platinum mesh were used as the reference and counter electrodes, respectively. The electrolytes were Ar-saturated 0.1 M KOH (pH 13) containing different concentrations of NO_3^- . The electrochemical cell was maintained in an Ar atmosphere during experiments. The LSV curves were collected at a scan rate of 5 mV s^{-1} . All potentials were calibrated to the RHE reference scale using $E_{\text{RHE}} = E_{\text{Ag/AgCl}} + 0.207\text{V} + 0.0591 \times \text{pH}$. The current density was normalized to the geometric electrode area (~ 0.5 cm^2). Note that the electrode area was 0.2 cm^2 for tests in 0.05 and 0.1 M nitrate. The solution resistance (R_s) was measured using potentiostatic electrochemical impedance spectroscopy with a frequency range of 0.1 Hz to 200 kHz and an amplitude of 10 mV_{pp}. The potentials were compensated by iR_s -drop from the electrolyte resistance. Potentiostatic measurements were performed for 1 h in 30 ml cathode electrolyte with a stirring rate of 300 rpm, and then the electrolyte was stored at 4°C (no more than 2 days) before analysis. To assess the performance change of CuCoSP during ten cycles of one-hour electrolysis at -0.175 V (vs. RHE), the electrolyte (30 ml, 0.1 M KOH and 0.01 M nitrate) was collected after each one-hour electrolysis for product analysis and a fresh electrolyte was used for the next cycle of one-hour electrolysis. Note that NH_3 volatilization in the electrolytes (pH 13) is negligible during the one-hour electrolysis (Supplementary Fig. S19). The C_{dl} was determined by CV scanning in a non-faradaic potential window at different scan rates (10 – 120 mV s^{-1}). The plot of capacitive anode and cathode current differences ($[j_{\text{a}} - j_{\text{c}}]/2$) at a set potential against the CV scan rates shows a linear relationship, and the slope is C_{dl} .

Kinetic evaluation. The LSVs of the catalysts were recorded at a scan rate of 1 mV s^{-1} in 0.1 M KOH (pH 13) containing 0.01 M NO_3^- or 0.01 M NO_2^- (KNO_3 , $\geq 96\%$). To obtain the rate constant, the electrolysis at -0.175 V (vs. RHE) were performed for 1 h in 22 ml electrolyte (0.1 M KOH) containing 0.01 M NO_3^- or 0.01 M NO_2^- in the cathode chamber. The reaction constant (k_1 for NO_3^- reduction and k_2 for NO_2^- reduction) was obtained by monitoring the concentration evolution of NO_3^- or NO_2^- ions as a function of electrolysis time, assuming that their concentrations decayed exponentially as per first-order rate, that is, $C_t = C_0 \exp(-k \times t)$, where C_0 is the initial molar concentration of reactant (NO_3^- or NO_2^-) and C_t is the molar concentration of reactant at time t .

Determination of ion concentrations

NH_4^+ quantification. The produced NH_3 was quantitatively determined using the indophenol blue method^{10,69}. Typically, a certain amount of electrolyte was taken out from the reaction cell and diluted to 2 ml. Then, 2 ml of 1 M NaOH ($\geq 98\%$) solution containing sodium citrate ($\geq 99\%$) and salicylic acid ($\geq 99\%$) (stored at 4°C) and 1 ml of freshly prepared 0.05 M NaClO was added. The mixed solution was shaken for few seconds. Finally, 0.2 ml of 1 wt.% sodium nitroferriyanide ($\geq 99\%$) solution (stored at 4°C) were added for the colour reaction. After keeping at room temperature for 1 h, the resulting solution was measured using an ultraviolet-visible (UV-Vis) spectrophotometer. The absorbance at ~ 655 nm was used to determine the concentration of NH_3 . In order to quantify the amount of NH_3 , a calibration curve was built using standard NH_4Cl ($\geq 99.5\%$) solution in 0.1 M KOH.

NO_2^- quantification⁴⁴. A specific colour reagent for NO_2^- quantification was prepared by mixing 0.20 g of N-(1-naphthyl) ethylenediamine dihydrochloride ($\geq 98\%$), 4.0 g of sulfonamide ($\geq 99\%$) and 10 ml of phosphoric acid (85 wt.% in H_2O) ($\rho = 1.7$ g/ml) with 50 ml of deionized water. In a typical colorimetric test, 1 ml HCl (1 M) was firstly added into the 5 ml of diluted post-electrolysis electrolytes, and then 0.1 ml of colour reagent was added and shaken to obtain a uniform solution. The UV-Vis absorbance at 540 nm was recorded after 20 min at room temperature. The amount of NO_2^- was determined using a calibration curve of NaNO_2 ($\geq 96\%$) solutions. N_2H_4 and NH_2OH were probably produced during the electroreduction of nitrate. However, their concentrations are expected to be very low and only measurable at intermediate times, owing to their high reactivity in basic media^{42,43}. Thus, we mainly focused on analyzing the yields of NH_3 and NO_2^- .

NO_3^- quantification^{44,83}. A certain amount of post-electrolysis electrolytes was diluted to 4 ml. Then, 1 ml of 1 M HCl and 0.1 ml sulfamic acid (98%) solution (0.8 wt.%) were added, and the final mixed solution was shaken to obtain a uniform solution. UV-Vis spectrophotometer was used to record the absorption intensities at wavelengths of 220 nm and 275 nm. The calculated absorbance value A ($A = A_{220\text{nm}} - 2 \times A_{275\text{nm}}$) is linearly related to the NO_3^- concentrations. In order to quantify the amount of NO_3^- , a calibration curve was obtained using KNO_3 standard solution.

Calculation of the FE, Y_{NH_3} and j_{NH_3} . The FE was defined as the charge consumed for the formation of a specific product (e.g., NH_3) divided by the total charge passing

through the electrodes (Q) during electrolysis. Given that eight electrons are consumed to produce one NH₃ molecule, the FE of NH₃ (FE_{NH_3}), Y_{NH_3} and j_{NH_3} can be calculated as follows: $FE_{\text{NH}_3} = (8 \times F \times C_{\text{NH}_3} \times V) / Q$, $Y_{\text{NH}_3} = (C_{\text{NH}_3} \times V) / (A \times t)$, and $j_{\text{NH}_3} = (Q \times FE_{\text{NH}_3}) / (A \times t)$, where F is the Faraday constant, C_{NH_3} is the molar concentration of detected NH₃, V is the volume of the electrolytes, A is the electrode geometric area, and t is the reaction time. Given that two electrons are consumed to produce one NO₂⁻ molecule, the FE of NO₂⁻ can be calculated as follows: $FE(\text{NO}_2^-) = (2 \times F \times C(\text{NO}_2^-) \times V) / Q$, where $C(\text{NO}_2^-)$ is the molar concentration of detected NO₂⁻.

¹⁵NO₃⁻ Isotope labelling experiments and ¹⁴NH₃ quantification by ¹H NMR.

To quantify the ¹⁴NH₄⁺ yield after electrolysis of 0.01 M K¹⁴NO₃ at -0.175 V (vs. RHE) for 1 h, a calibration curve of ¹H NMR (400 MHz) measurements was constructed using a series of ¹⁴NH₄Cl solutions with defined concentrations (1, 2, 3, 4 and 5 mM) as standards. In a typical procedure⁸⁴, 125 μl of the standard solution/electrolytes was mixed with 125 μl of 15 mM maleic acid in DMSO-D₆ (99.9 atom% D), 50 μl of 4 M H₂SO₄ in DMSO-D₆ and 750 μl of DMSO-D₆. The peak area integral ratio of ¹⁴NH₄⁺ to maleic acid is positively correlated with the concentrations of ¹⁴NH₄⁺. To confirm the source of NH₃ qualitatively, 0.01 M Na¹⁵NO₃ (>98 atom% ¹⁵N, ≥99% purity) and 0.1 M KOH were used as the feeding electrolytes for 1 h electrolysis at -0.175 V (vs. RHE) and ¹⁵NH₄⁺ in the electrolyte was detected using ¹H NMR⁸⁴.

Operando SECM test. To prepare the model catalyst, a CuSP slid (0.5 × 3 cm²) was cleaned using 0.1 M HCl under ultrasonication for 20 min, washed by deionized water, and dried by blotting paper. Then, half of the CuSP slid was immersed in a MOFs growth solution (a mixture of 1.5 ml of 2-methylimidazole (0.4 M) and 1.5 ml aqueous solution of Co(NO₃)₂ · 6H₂O (50 mM)) in Ar-atmosphere for 6 h. The formed Cu₂ZIF-Co hybrid layers were washed with deionized water, dried with blotting paper, and further immersed in 1 M KOH solution bubbled with Ar gas for 1.5 h in a gas-tight cell, during which the ZIF-Co film was completely converted into a uniform and compacted Co(OH)₂ layer, due to the poor stability of ZIF-Co MOFs in water⁸⁵. After washed with water and ethanol and drying at 25 °C, half of the CuSP slide was exposed in Air and the other half was covered by Co(OH)₂ nanosheets, both of which constitute the Cu (CuO_x)₂Co(OH)₂ model catalyst.

The SECM setup with shear-force-based distance control is located in a faraday cage to allow for shielding of electrical noise, with the exception of the lock-in amplifier and the potentiostat^{86,87}. During the SECM measurements, the Cu₂Co(OH)₂ catalyst were used as the sample (working electrode 1; WE 1), while a Pt-UME with a diameter of ~1 μm (working electrode 2; WE 2), Ag/AgCl/3 M KCl (reference electrode) and a Pt-mesh (counter electrode separated by a Zirfon membrane) were assembled to a four-electrode system. The sample was polarized to -0.12 V (vs. RHE) for triggering the NO₃RR, while at the Pt-UME cyclic voltammograms were performed in a potential range between -0.12 V and 1.58 V (vs. RHE) at a scan rate of 200 mV s⁻¹ to identify intermediately formed NO₂⁻ (at 0.06 V vs. RHE) and NH₃ (at 0.76 V vs. RHE). Each SECM array scan was recorded from the Cu/CuO_x layer to the Co(OH)₂ layer with an overall x-displacement of 1200 μm, while the border between the two layers is at ~600 μm.

In situ Raman spectroscopy. Raman spectroscopy was performed with a Lab-RAM HR Raman microscopy system (Horiba Jobin Yvon, HR550) equipped with a 532 nm laser as the excitation source, a water immersion objective (Olympus LUMFL, 60×, numerical aperture = 1.10), a monochromator (1800 grooves/mm grating) and a Synapse CCD detector. Each spectrum is an average of five continuously acquired spectra with a collection time of 50 s each. A three-electrode electrochemical cell was used for in situ Raman tests. Pt wires and Ag/AgCl (3 M KCl) were used as counter and reference electrodes, respectively. To protect the objective from the corrosive 0.1 M KOH electrolyte, 0.01 M KOH (pH 12) was used instead. K₂SO₄ (≥99.0%) was added to ensure sufficient ionic conductivity (keeping the total concentration of K⁺ to be 0.1 M) and provides SO₄²⁻ ions as an external Raman reference. Typically, in the presence of 0.01 M KNO₃, the supporting electrolytes were 0.01 M KOH and 0.04 M K₂SO₄. In the absence of KNO₃, the electrolytes were 0.01 M KOH and 0.045 M K₂SO₄.

Data availability

The data generated and analyzed during this study are provided in the main text and Supplementary information file or can be obtained from the corresponding authors on reasonable request.

Received: 28 August 2021; Accepted: 8 February 2022;

Published online: 02 March 2022

References

1. Foster, S. L. et al. Catalysts for nitrogen reduction to ammonia. *Nat. Catal.* **1**, 490–500 (2018).

- Ashida, Y., Arashiba, K., Nakajima, K. & Nishibayashi, Y. Molybdenum-catalysed ammonia production with samarium diiodide and alcohols or water. *Nature* **568**, 536–540 (2019).
- Tang, C. & Qiao, S. -Z. How to explore ambient electrocatalytic nitrogen reduction reliably and insightfully. *Chem. Soc. Rev.* **48**, 3166–3180 (2019).
- Kitano, M. et al. Ammonia synthesis using a stable electride as an electron donor and reversible hydrogen store. *Nat. Chem.* **4**, 934–940 (2012).
- Martin, A. J., Shinagawa, T. & Pérez-Ramírez, J. Electrocatalytic reduction of nitrogen: From Haber–Bosch to ammonia artificial leaf. *Chem* **5**, 263–283 (2019).
- Guo, C., Ran, J., Vasileff, A. & Qiao, S. -Z. Rational design of electrocatalysts and photo(electro)catalysts for nitrogen reduction to ammonia (NH₃) under ambient conditions. *Energy Environ. Sci.* **11**, 45–56 (2018).
- Soloveichik, G. Electrochemical synthesis of ammonia as a potential alternative to the Haber–Bosch process. *Nat. Catal.* **2**, 377–380 (2019).
- Wan, Y., Xu, J. & Lv, R. Heterogeneous electrocatalysts design for nitrogen reduction reaction under ambient conditions. *Mater. Today* **27**, 69–90 (2019).
- Cui, X., Tang, C. & Zhang, Q. A review of electrocatalytic reduction of dinitrogen to ammonia under ambient conditions. *Adv. Energy Mater.* **8**, 1800369 (2018).
- Wang, J. et al. Ambient ammonia synthesis via palladium-catalyzed electrohydrogenation of dinitrogen at low overpotential. *Nat. Commun.* **9**, 1795 (2018).
- Chen, P. et al. Interfacial engineering of cobalt sulfide/graphene hybrids for highly efficient ammonia electrosynthesis. *Proc. Natl Acad. Sci. USA* **116**, 6635–6640 (2019).
- Song, Y. et al. A physical catalyst for the electrolysis of nitrogen to ammonia. *Sci. Adv.* **4**, e1700336 (2018).
- Lv, C. et al. An amorphous noble-metal-free electrocatalyst that enables nitrogen fixation under ambient conditions. *Angew. Chem. Int. Ed.* **57**, 6073–6076 (2018).
- Li, S. -J. et al. Amorphizing of Au Nanoparticles by CeO_x-RGO hybrid support towards highly efficient electrocatalyst for N₂ reduction under ambient conditions. *Adv. Mater.* **29**, 1700001 (2017).
- Geng, Z. et al. Achieving a record-high yield rate of 120.9 μg_{NH₃} mg_{cat}⁻¹ h⁻¹ for N₂ electrochemical reduction over Ru single-atom catalysts. *Adv. Mater.* **30**, 1803498 (2018).
- Chen, G. -F. et al. Ammonia electrosynthesis with high selectivity under ambient conditions via a Li⁺ incorporation strategy. *J. Am. Chem. Soc.* **139**, 9771–9774 (2017).
- Rosca, V., Duca, M., de Groot, M. T. & Koper, M. T. M. Nitrogen cycle electrocatalysis. *Chem. Rev.* **109**, 2209–2244 (2009).
- Chen, J. G. et al. Beyond fossil fuel-driven nitrogen transformations. *Science* **360**, eaar6611 (2018).
- Long, J. et al. Direct electrochemical ammonia synthesis from nitric oxide. *Angew. Chem. Int. Ed.* **59**, 9711–9718 (2020).
- Wang, Y., Yu, Y., Jia, R., Zhang, C. & Zhang, B. Electrochemical synthesis of nitric acid from air and ammonia through waste utilization. *Natl Sci. Rev.* **6**, 730–738 (2019).
- van Langevelde, P. H., Katsounaros, I. & Koper, M. T. M. Electrocatalytic nitrate reduction for sustainable ammonia production. *Joule* **5**, 290–294 (2021).
- McEnaney, J. M. et al. Electrolyte engineering for efficient electrochemical nitrate reduction to ammonia on a titanium electrode. *ACS Sustain. Chem. Eng.* **8**, 2672–2681 (2020).
- Hao, D. et al. Emerging alternative for artificial ammonia synthesis through catalytic nitrate reduction. *J. Mater. Res. Technol.* **77**, 163–168 (2021).
- Katsounaros, I. On the assessment of electrocatalysts for nitrate reduction. *Curr. Opin. Electrochem.* **28**, 100721 (2021).
- Wu, Z. -Y. et al. Electrochemical ammonia synthesis via nitrate reduction on Fe single atom catalyst. *Nat. Commun.* **12**, 2870 (2021).
- Yu, Y., Wang, C., Yu, Y., Wang, Y. & Zhang, B. Promoting selective electroreduction of nitrates to ammonia over electron-deficient Co modulated by rectifying Schottky contacts. *Sci. China Chem.* **63**, 1469–1476 (2020).
- Sun, J. et al. A hybrid plasma electrocatalytic process for sustainable ammonia production. *Energy Environ. Sci.* **14**, 865–872 (2021).
- Li, L. et al. Efficient nitrogen fixation to ammonia through integration of plasma oxidation with electrocatalytic reduction. *Angew. Chem. Int. Ed.* **60**, 14131–14137 (2021).
- Milton, R. D. & Minter, S. D. Enzymatic bioelectrosynthetic ammonia production: recent electrochemistry of nitrogenase, nitrate reductase, and nitrite reductase. *ChemPlusChem* **82**, 513–521 (2017).
- Duca, M., Weeks, J. R., Fedor, J. G., Weiner, J. H. & Vincent, K. A. Combining noble metals and enzymes for relay cascade electrocatalysis of nitrate reduction to ammonia at neutral pH. *ChemElectroChem* **2**, 1086–1089 (2015).
- Ford, C. L., Park, Y. J., Matson, E. M., Gordon, Z. & Fout, A. R. A bioinspired iron catalyst for nitrate and perchlorate reduction. *Science* **354**, 741–743 (2016).

32. Coelho, C. & Romão, M. J. Structural and mechanistic insights on nitrate reductases. *Protein Sci.* **24**, 1901–1911 (2015).
33. Harris, L. E. The lower electronic states of nitrite and nitrate ion, nitromethane, nitramide, nitric acid, and nitrate esters. *J. Chem. Phys.* **58**, 5615–5626 (1973).
34. Li, Y. et al. Enzyme mimetic active intermediates for nitrate reduction in neutral aqueous media. *Angew. Chem. Int. Ed.* **59**, 9744–9750 (2020).
35. Wang, Z., Richards, D. & Singh, N. Recent discoveries in the reaction mechanism of heterogeneous electrocatalytic nitrate reduction. *Catal. Sci. Technol.* **11**, 705–725 (2021).
36. Duca, M. & Koper, M. T. M. Powering denitrification: the perspectives of electrocatalytic nitrate reduction. *Energy Environ. Sci.* **5**, 9726–9742 (2012).
37. Liu, J. -X., Richards, D., Singh, N. & Goldsmith, B. R. Activity and selectivity trends in electrocatalytic nitrate reduction on transition metals. *ACS Catal.* **9**, 7052–7064 (2019).
38. Wang, S. et al. Universal transition state scaling relations for (de) hydrogenation over transition metals. *Phys. Chem. Chem. Phys.* **13**, 20760–20765 (2011).
39. Li, F. et al. Cooperative CO₂-to-ethanol conversion via enriched intermediates at molecule–metal catalyst interfaces. *Nat. Catal.* **3**, 75–82 (2020).
40. Martinez, J., Ortiz, A. & Ortiz, I. State-of-the-art and perspectives of the catalytic and electrocatalytic reduction of aqueous nitrates. *Appl. Catal. B: Environ.* **207**, 42–59 (2017).
41. Zhang, X. et al. Recent advances in non-noble metal electrocatalysts for nitrate reduction. *Chem. Eng. J.* **403**, 126269 (2021).
42. Pérez-Gallent, E., Figueiredo, M. C., Katsounaros, I. & Koper, M. T. M. Electrocatalytic reduction of nitrate on copper single crystals in acidic and alkaline solutions. *Electrochim. Acta* **227**, 77–84 (2017).
43. Reyter, D., Bélanger, D. & Roué, L. Study of the electroreduction of nitrate on copper in alkaline solution. *Electrochim. Acta* **53**, 5977–5984 (2008).
44. Wang, Y., Zhou, W., Jia, R., Yu, Y. & Zhang, B. Unveiling the activity origin of a copper-based electrocatalyst for selective nitrate reduction to ammonia. *Angew. Chem. Int. Ed.* **59**, 5350–5354 (2020).
45. Wang, Y. et al. Enhanced nitrate-to-ammonia activity on copper–nickel alloys via tuning of intermediate adsorption. *J. Am. Chem. Soc.* **142**, 5702–5708 (2020).
46. Lu, C., Lu, S., Qiu, W. & Liu, Q. Electroreduction of nitrate to ammonia in alkaline solutions using hydrogen storage alloy cathodes. *Electrochim. Acta* **44**, 2193–2197 (1999).
47. Durivault, L. et al. Cu–Ni materials prepared by mechanical milling: their properties and electrocatalytic activity towards nitrate reduction in alkaline medium. *J. Alloy. Compd.* **432**, 323–332 (2007).
48. Dima, G. E., de Vooy, A. C. A. & Koper, M. T. M. Electrocatalytic reduction of nitrate at low concentration on coinage and transition–metal electrodes in acid solutions. *J. Electroanal. Chem.* **554–555**, 15–23 (2003).
49. Su, J. F., Ruzibayev, I., Shah, I. & Huang, C. P. The electrochemical reduction of nitrate over micro-architected metal electrodes with stainless steel scaffold. *Appl. Catal. B: Environ.* **180**, 199–209 (2016).
50. Reyter, D., Chamoulaud, G., Bélanger, D. & Roué, L. Electrocatalytic reduction of nitrate on copper electrodes prepared by high-energy ball milling. *J. Electroanal. Chem.* **596**, 13–24 (2006).
51. Chen, G. -F. et al. Electrochemical reduction of nitrate to ammonia via direct eight–electron transfer using a copper–molecular solid catalyst. *Nat. Energy* **5**, 605–613 (2020).
52. Li, J. et al. Efficient ammonia electrosynthesis from nitrate on strained ruthenium nanoclusters. *J. Am. Chem. Soc.* **142**, 7036–7046 (2020).
53. Zhao, Y. et al. Speciation of Cu surfaces during the electrochemical CO reduction reaction. *J. Am. Chem. Soc.* **142**, 9735–9743 (2020).
54. Deng, Y., Handoko, A. D., Du, Y., Xi, S. & Yeo, B. S. In situ Raman spectroscopy of copper and copper oxide surfaces during electrochemical oxygen evolution reaction: identification of Cu^{III} oxides as catalytically active species. *ACS Catal.* **6**, 2473–2481 (2016).
55. Wang, L. et al. Migration of cobalt species within mixed platinum–cobalt oxide bifunctional electrocatalysts in alkaline electrolytes. *J. Electrochem. Soc.* **166**, F3093–F3097 (2019).
56. Zheng, W., Liu, M. & Lee, L. Y. S. Electrochemical instability of metal–organic frameworks: In situ spectroelectrochemical investigation of the real active sites. *ACS Catal.* **10**, 81–92 (2020).
57. Mefford, J. T. et al. Correlative operando microscopy of oxygen evolution electrocatalysts. *Nature* **593**, 67–73 (2021).
58. Wang, J., Tan, H. -Y., Zhu, Y., Chu, H. & Chen, H. M. Linking the dynamic chemical state of catalysts with the product profile of electrocatalytic CO₂ reduction. *Angew. Chem. Int. Ed.* **60**, 17254–17267 (2021).
59. Morales–Guio, C. G. et al. Improved CO₂ reduction activity towards C₂₊ alcohols on a tandem gold on copper electrocatalyst. *Nat. Catal.* **1**, 764–771 (2018).
60. Yan, H. et al. Tandem In₂O₃–Pt/Al₂O₃ catalyst for coupling of propane dehydrogenation to selective H₂ combustion. *Science* **371**, 1257–1260 (2021).
61. Yamada, Y. et al. Nanocrystal bilayer for tandem catalysis. *Nat. Chem.* **3**, 372–376 (2011).
62. O'Mara, P. B. et al. Cascade reactions in nanozymes: spatially separated active sites inside Ag-core-porous-Cu-shell nanoparticles for multistep carbon dioxide reduction to higher organic molecules. *J. Am. Chem. Soc.* **141**, 14093–14097 (2019).
63. Fajardo, A. S., Westerhoff, P., Sanchez-Sanchez, C. M. & Garcia–Segura, S. Earth–abundant elements a sustainable solution for electrocatalytic reduction of nitrate. *Appl. Catal. B: Environ.* **281**, 119465 (2021).
64. Guo, Y., Stroka, J. R., Kandemir, B., Dickerson, C. E. & Bren, K. L. Cobalt metalloprotein electrocatalyst for the selective reduction of nitrite to ammonium. *J. Am. Chem. Soc.* **140**, 16888–16892 (2018).
65. He, W., Ifraemov, R., Raslin, A. & Hod, I. Room-temperature electrochemical conversion of metal–organic frameworks into porous amorphous metal sulfides with tailored composition and hydrogen evolution activity. *Adv. Funct. Mater.* **28**, 1707244 (2018).
66. He, W., Liberman, I., Rozenberg, I., Ifraemov, R. & Hod, I. electrochemically driven cation exchange enables the rational design of active CO₂ reduction electrocatalysts. *Angew. Chem. Int. Ed.* **59**, 8262–8269 (2020).
67. Liberman, I., He, W., Shimoni, R., Ifraemov, R. & Hod, I. Spatially confined electrochemical conversion of metal–organic frameworks into metal–sulfides and their in situ electrocatalytic investigation via scanning electrochemical microscopy. *Chem. Sci.* **11**, 180–185 (2020).
68. Choi, J. et al. Identification and elimination of false positives in electrochemical nitrogen reduction studies. *Nat. Commun.* **11**, 5546 (2020).
69. Zhao, Y. et al. Ammonia detection methods in photocatalytic and electrocatalytic experiments: How to improve the reliability of NH₃ production rates? *Adv. Sci.* **6**, 1802109 (2019).
70. Lefebvre, M. C. In *Modern Aspects of Electrochemistry* (eds Conway, B. E. et al.) 249–300 (Springer USA, 2002).
71. Fang, Y. -H. & Liu, Z. -P. Tafel kinetics of electrocatalytic reactions: from experiment to first-principles. *ACS Catal.* **4**, 4364–4376 (2014).
72. Petrii, O. A., Nazmutdinov, R. R., Bronshtein, M. D. & Tsilina, G. A. Life of the tafel equation: Current understanding and prospects for the second century. *Electrochim. Acta* **52**, 3493–3504 (2007).
73. Kim, H. et al. Operando stability of platinum electrocatalysts in ammonia oxidation reactions. *ACS Catal.* **10**, 11674–11684 (2020).
74. Duca, M. et al. New insights into the mechanism of nitrite reduction on a platinum electrode. *J. Electroanal. Chem.* **649**, 59–68 (2010).
75. Yang, J., Sebastian, P., Duca, M., Hoogenboom, T. & Koper, M. T. M. pH dependence of the electroreduction of nitrate on Rh and Pt polycrystalline electrodes. *Chem. Commun.* **50**, 2148–2151 (2014).
76. Krylova, V. & Andrulevičius, M. Optical, XPS and XRD studies of semiconducting copper sulfide layers on a polyamide film. *Int. J. Photoenergy* **2009**, 304308 (2009).
77. Rivas–Murias, B. & Salgueiriño, V. Thermodynamic CoO–Co₃O₄ crossover using Raman spectroscopy in magnetic octahedron–shaped nanocrystals. *J. Raman Spectrosc.* **48**, 837–841 (2017).
78. Yang, J., Liu, H., Martens, W. N. & Frost, R. L. Synthesis and characterization of cobalt hydroxide, cobalt oxyhydroxide, and cobalt oxide nanodiscs. *J. Phys. Chem. C* **114**, 111–119 (2010).
79. Liu, Y. -C., Koza, J. A. & Switzer, J. A. Conversion of electrodeposited Co(OH)₂ to CoOOH and Co₃O₄, and comparison of their catalytic activity for the oxygen evolution reaction. *Electrochim. Acta* **140**, 359–365 (2014).
80. Dupin, J. -C., Gonbeau, D., Vinatier, P. & Levasseur, A. Systematic XPS studies of metal oxides, hydroxides and peroxides. *Phys. Chem. Chem. Phys.* **2**, 1319–1324 (2000).
81. Xu, M., Larentzos, J. P., Roshdy, M., Criscenti, L. J. & Allen, H. C. Aqueous divalent metal–nitrate interactions: hydration versus ion pairing. *Phys. Chem. Chem. Phys.* **10**, 4793–4801 (2008).
82. Hanifpour, F., Sveinbjörnsson, A., Canales, C. P., Skúlason, E. & Flosadóttir, H. D. Preparation of Nafion membranes for reproducible ammonia quantification in nitrogen reduction reaction experiments. *Angew. Chem. Int. Ed.* **59**, 22938–22942 (2020).
83. Bastian, R., Weberling, R. & Palilla, F. Ultraviolet spectrophotometric determination of nitrate: application to analysis of alkaline carbonates. *Anal. Chem.* **29**, 1795–1797 (1957).
84. Hodgetts, R. Y. et al. Refining universal procedures for ammonium quantification via rapid ¹H NMR analysis for dinitrogen reduction studies. *ACS Energy Lett.* **5**, 736–741 (2020).
85. Zhou, K. et al. Characterization and properties of Zn/Co zeolitic imidazolate frameworks vs. ZIF-8 and ZIF-67. *J. Mater. Chem. A* **5**, 952–957 (2017).
86. Dieckhöfer, S. et al. Probing the local reaction environment during high turnover carbon dioxide reduction with Ag-based gas diffusion electrodes. *Chem. Eur. J.* **27**, 5906–5912 (2021).
87. Monteiro, M. C. O. et al. Probing the local activity of CO₂ reduction on gold gas diffusion electrodes: effect of the catalyst loading and CO₂ pressure. *Chem. Sci.* **12**, 15682–15690 (2021).

Acknowledgements

This project has received funding from the European Research Council (ERC) under the European Union's Horizon 2020 research and innovation programme (grant agreement CasCat [833408]) and in the framework of the Marie Skłodowska–Curie MSCA-ITN “Implantsens” [813006] as well as from the Deutsche Forschungsgemeinschaft (DFG, German Research Foundation) under Germany's Excellence Strategy-EXC 2033-390677874-RESOLV and the “Center for Solvation Science ZEMOS” funded by the German Federal Ministry of Education and Research BMBF and by the Ministry of Culture and Research of Nord Rhine–Westphalia is acknowledged.

Author contributions

W.S. supervised this project. W.S. and W.H. conceived the project. W.H. conducted the experiments. J.Z. performed the TEM measurements. S.D. performed the XPS and SECM measurements. S.V. performed the SEM and EDS measurements. W.H. and A.C.B. performed the Raman measurements. J.R.C.J. and A.L. performed the ^1H NMR measurements. S.S. carried out the XRD measurements. All authors contributed to the data analysis. W.S. and W.H. wrote the paper.

Funding

Open Access funding enabled and organized by Projekt DEAL.

Competing interests

The authors declare no competing interests.

Additional information

Supplementary information The online version contains supplementary material available at <https://doi.org/10.1038/s41467-022-28728-4>.

Correspondence and requests for materials should be addressed to Wolfgang Schuhmann.

Peer review information *Nature Communications* thanks Hoang-Long Du, Seung Woo Lee, Sergi Garcia-Segura, Zhong-Qun Tian and the other anonymous reviewer(s) for their contribution to the peer review of this work.

Reprints and permission information is available at <http://www.nature.com/reprints>

Publisher's note Springer Nature remains neutral with regard to jurisdictional claims in published maps and institutional affiliations.



Open Access This article is licensed under a Creative Commons Attribution 4.0 International License, which permits use, sharing, adaptation, distribution and reproduction in any medium or format, as long as you give appropriate credit to the original author(s) and the source, provide a link to the Creative Commons license, and indicate if changes were made. The images or other third party material in this article are included in the article's Creative Commons license, unless indicated otherwise in a credit line to the material. If material is not included in the article's Creative Commons license and your intended use is not permitted by statutory regulation or exceeds the permitted use, you will need to obtain permission directly from the copyright holder. To view a copy of this license, visit <http://creativecommons.org/licenses/by/4.0/>.

© The Author(s) 2022